A SIMPLE ANALYTICAL FUSELAGE-INDUCED VELOCITY MODEL FOR COMPREHENSIVE ROTOR CODES

Berend G. van der Wall[*], Marc Wentrup[**], Ganesh Rajagopalan[***], Sung N. Jung[****]
[*] Institute of Flight Systems, DLR Braunschweig, Germany
[**] Institute of Aerodynamics and Flow Technology, DLR Braunschweig, Germany
[***] Department of Aerospace Engineering, Iowa State University, Ames, IA, US
[****] Department of Aerospace Engineering, Konkuk University, Seoul, Korea

Abstract

A simple analytical model to account for fuselage-induced velocities at rotor blade elements and at rotor wake nodes is described. The method is applied to three different fuselage configurations. Results obtained with a comprehensive rotor code show the fuselage effect on rotor trim controls, comparing the isolated rotor with inclusion of the fuselage for the same trim. This is compared to a simple analytical estimate of the fuselage effect using blade element/momentum theory. It is found that in forward flight the lateral control is mainly affected by fuselage effects. Rotor thrust can be varied by the presence of the fuselage, depending on its angle of attack, and the fuselage influence generally increases with flight speed.

Nomenclature

A, B	Non-dimensional begin and end of the aerodynamic part of the blade
$A, A_0, etc.$	Magnitude and its coefficients of induced velocity function
c_{nj}	Polynomial coefficients
C_T, C_W	Thrust and weight coefficient
f_α, f_β	Interpolation factors
M_∞	Mach number
R, r	Radius, non-dimensional radial coordinate
$S_{A0}, etc.$	Shape parameter A in z-direction
$S_x, S_y, S_{x0}, S_{y0}, etc.$	Shape parameters in x and y direction and their coefficients
u, d, t	Subscripts denoting upwash, downwash and tail boom contributions
V_∞	Free-stream velocity
V_T, V_P	Velocity tangential and perpendicular to rotor blade section
v_{izf}	Fuselage-induced velocity in z-direction
x, y, z	Shaft-fixed coordinate system, origin in rotor hub
x_0, y_0	Coordinates of induced velocity peaks
z_0	Coordinate of fuselage centerline below the hub
α, β	Fuselage angle of attack, side-slip angle
α_a	Blade element angle of atack
$\Theta, \Theta_S, \Theta_C$	Blade pitch angle, longitudinal and lateral control angle
λ_{izf}	Non-dimensional fuselage-induced velocity, referenced to V_∞
μ	Rotor advance ratio
σ	Rotor solidity
ψ	Rotor blade azimuth angle
Ω	Rotor rotational speed

1. INTRODUCTION

Rotorcraft comprehensive codes are used for detailed flight mechanics, aerodynamics, dynamics and acoustics research. They usually include separate sophisticated models for each component, like two-dimensional unsteady blade section aerodynamics, beam theory for elastic blade motion, free-wake for the rotor-induced velocities, tabulated aerodynamic characteristics for the fuselage, and other component models. Interactions between these components – and others obstacles like ground, buildings, trees, other aircraft – often are either ignored, or significantly simplified, or introduced by means of any type of computational fluid dynamics (CFD) code of low order (panel methods, for example [1]) to high fidelity (Navier-Stokes solvers) at the expense of medium to huge additional computational effort. A good overview of the multitude of interactions is given by Sheridan [2].

In this paper, only the interaction between the fuselage and the rotor is addressed in this unidirectional sense (the reverse interaction from the rotor to the fuselage is left for future studies). The problem is sketched in Fig. 1 (a). At any flight speed the fuselage causes the air to pass around it and thus to generate an upwash in the front half of the rotor disk and a downwash in the rear half of it. Since flight speeds of conventional helicopters are theoretically limited to 360 km/h (= 100 m/s, ≈ 200 kts) the Mach number does not exceed 0.3 and therefore this represents an incompressible flow.

The rotor is operating outside the boundary layer of the fuselage in the outer potential flow; therefore panel methods may well be applied for many opera-

tional conditions of interest. One such application was given in Stepniewski's textbook on helicopter aerodynamics [3] and the computed deflection of the free-stream flow is sketched in Fig. 1 (b).

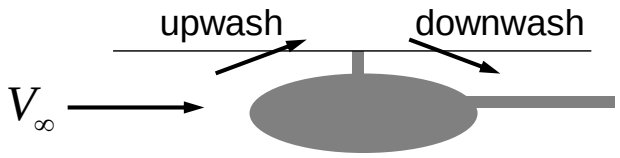

(a) Principle

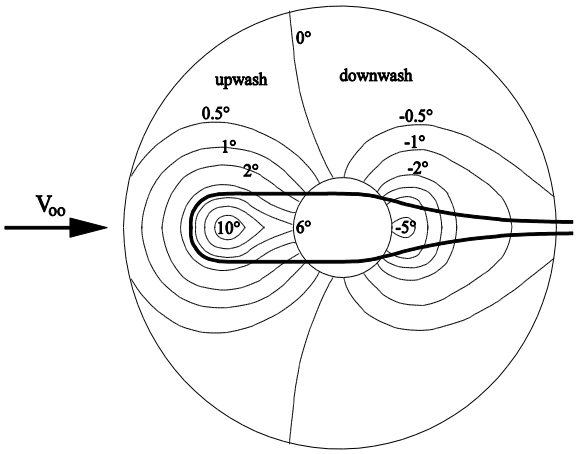

(b) Free-stream flow deflection, adapted from [3]

Fig. 1. Principle of fuselage-rotor interference.

Depending on the shape of the fuselage, the angle of attack towards the free-stream and the proximity of the rotor to it the local flow deflection may well exceed 10 deg and modify blade element aerodynamic loads significantly relative to an isolated rotor. An application using panel methods to investigate this effect for different rotor-fuselage separation distances was done by Huber [4]. It was found that the fuselage influence is highly non-linear with respect to the separation distance and that the fuselage significantly increases vibratory loads, compared to the isolated rotor. No data about how much trim controls or thrust are affected were given.

Many investigations regarding fuselage-rotor and rotor-fuselage interactions have been performed since then, nowadays mainly involving coupled computational structural dynamics and CFD solutions. It would exceed the scope of this paper to outline a review of all this work, and a comprehensive overview is found in [5]. Topics addressed were the impingement of the rotor wake on the fuselage, the variation of fuselage forces and moments due to the rotor and those of the rotor due to the presence of the fuselage, and effects of the fuselage on the wake convection. No attempt, however, was made to simplify the physical modeling in an engineering way and always some kind of CFD was used to compute those effects.

This paper tries to fill this gap and presents a simple analytical model of fuselage-induced velocities for the fuselage-rotor interference and the fuselage-wake interference, for usage at least in forward flight and descent conditions. The importance of interference models grows with the proximity of the rotor to the fuselage or to other interfering bodies like wings in compound designs [2], [6]. Fuselage-rotor interference can significantly degrade rotor performance and adversely affect vibration [4], [7]. To avoid this already in the pre-design phase where a large amount of parameter variations needs to be done using comprehensive analysis codes a simplified method to represent the fuselage-rotor interference effects is needed since in this stage of development CFD is unaffordable.

The solution proposed to this problem is the generation of a semi-empirical mathematical model that accounts for the specific fuselage flow field characteristics, the operational conditions, and the rotor-fuselage separation distances analytically. For this, a small set of isolated steady fuselage CFD computations is sufficient to generate a data base of fuselage-induced velocities within the volume defined by the rotor blade motion. This may involve either panel codes, Euler methods, or Reynolds-averaged Navier Stokes (RANS) CFD methods including flow separation.

Based on these data the parameters of the math model are identified. Then the model is ready for being used in comprehensive analysis without the need of further CFD computations. Because the model consists of a few lines of algebraic equations only, its evaluation is negligible in terms of computational effort compared to CFD and can be included in all the parameter variation studies without penalty.

Additional details on the modeling approach and results presented herein may be found in [8].

2. FUSELAGE MODELS AND CFD SETUP

Within this study three fuselages will be investigated:

- the Large Rotor Test Apparatus (LRTA),
- the smaller Rotor Test Apparatus (RTA),
- the Higher Harmonic Control Aeroacoustic Rotor Test (HART).

While the first two are used in the National Full-Scale Aerodynamics Complex (NFAC) at NASA Ames, California, the third one is used by DLR in the large low-speed facility of the German-Dutch wind tunnels in the Netherlands. All three of them are sketched with their dimensions in Fig. 2. Note that they are differently scaled; R is the rotor radius and z_0 is the position of the fuselage centerline below the hub center, which forms the origin of the coordinate system used.

The LRTA flow field is computed using the DLR TAU code, an unstructured compressible RANS solver [9], the RTA flow field by RotCFD, a structured incompressible RANS solver [10], and the HART fuselage by a structured compressible RANS solver KFLOW [11]. Due to the incompressibility character of the flow field the fuselage-induced velocities within the volume of rotor blade operation above the fuselage are linearly proportional to the wind speed V_∞. Thus, the most interesting component of the fuselage-induced velocities normal to the rotor disk, v_{izf}, can be made non-dimensional in the form v_{izf}/V_∞ which is independent of V_∞. Thus, only one appropriate free-stream velocity can be used in CFD computations. Different values were chosen for the various computations that were performed independently by the contributors. The air data for all the CFD computations are standard atmosphere at sea level and $15°C$ temperature.

In addition, the overall grid size and density was very different and a comparison of these data is given in Table 1.

The attitudes of the LRTA and RTA are limited to the range $-20° \leq \alpha \leq +15°$ and similar for the HART used in the DNW, however, for this fuselage CFD computations were performed in the range $-90° \leq \alpha \leq +90°$. $\alpha = -90°$ represents a vertical climb where the flow is attacking the fuselage from the top, as also is the case in hover due to the rotor downwash. $\alpha = -20°$ represents a steep climb, $\alpha = -10°$ either a moderate climb or high-speed level flight, $\alpha = 0°$ a low speed forward flight or high speed dive, $\alpha = +10°$ is characteristic for moderate to low speed descent, and finally $\alpha = +90°$ resembles a vertical descent for the fuselage. The settings where data were generated are also given in Table 1.

(a) LRTA for UH-60 size rotors ($R = 26.83\ ft = 8.179\ m$); $z_0/R = -0.2676$

(b) RTA for Bo105 size rotors ($R = 16.11\ ft = 4.91\ m$); $z_0/R = -0.4$

(c) HART for model-scale rotors ($R = 6.56\ ft = 2.0\ m$); $z_0/R = -0.3$

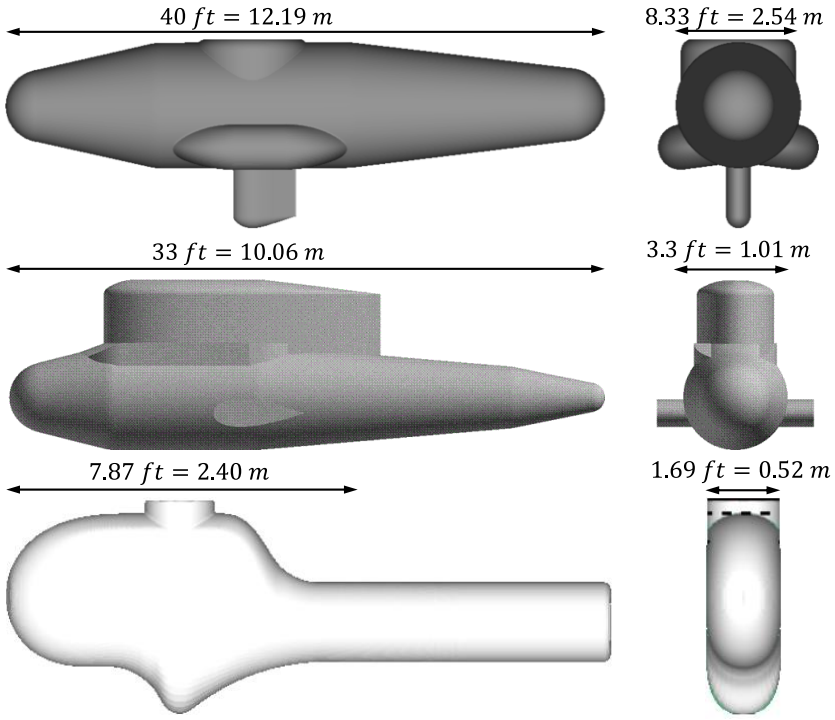

Fig. 2. Fuselage bodies investigated.

Table 1: Parameters used in CFD computations.

Fuselage (code used)	LRTA (TAU)	RTA (RotCFD)	HART (KFLOW)
Compressible	yes	no	yes
Solution type	steady RANS	steady RANS	steady RANS
Grid type	unstructured	structured	structured
Outer grid size, multiples of R	149.1	248.3	10
Total discretization, times 10^6	2.2 (points)	0.066 (cells)	31.5 (cells)
Free-stream velocity, V_∞	$50\ m/s$	$51.4\ m/s$	$32.9\ m/s$
Free-stream Mach number, M_∞	0.147	0.151	0.097
Angles of attack computed, α	$-20°, \pm 15°, \pm 10°, \pm 5°, 0°$	$-20°, \pm 15°, \pm 10°, \pm 5°, 0°$	$\pm 90°, \pm 60°, \pm 30°, \pm 10°, 0°$

The reason for using steady RANS instead of unsteady RANS is found in the application of the results: the goal is to create a mathematical model for the steady mean characteristics of the flow field. Unsteady RANS will result in highly unsteady flow fields when flow separation occurs, which usually is the case when bluff bodies are being computed, such as helicopter fuselages. Unsteady results need a long-term averaging procedure to obtain averaged flow field characteristics. In addition, the steady RANS is computationally much faster and thus more efficient for the purposes of this study. For the moderate angles of attack in case of LRTA and RTA no severe flow separation took place, but the more extreme settings in case of HART caused strong flow separation on the leeward side of the fuselage.

Data extraction for generating the math model was confined to the volume defined by the rotor blade operation. Assuming a typical coning of $3°$ and a $1/rev$ blade flapping with relatively large amplitude of $8°$ this volume can be defined by the following cuboid in shaft axis coordinates, with x pointing downstream, y to the starboard side and z upwards in rotor shaft direction: $-1 \leq x/R, y/R \leq +1$ and $-0.1 \leq z/R \leq +0.2$ with origin in the hub center. Data were extracted in four planes within this volume $z/R = -0.1, 0, 0.1, 0.2$ with a resolution of 65 equidistant samples (LRTA, RTA) or 84 (HART) in each x, y direction.

Only in HART the flow separation effects affected the extracted data for angles of attack $\alpha \geq 0°$. Due to the rounded surface the separation line was pulsating and the CFD solution was unsteady. This required special attention when fitting the math model to the data field since these unsteady disturbances need to be eliminated from the parameter identification process for a model that is supposed to represent the time-averaged steady flow field.

Additionally to the main fuselage body the HART had a rearward sting adapter which was relatively thick in diameter and which covered the outer half rotor radius in the rear position. For angles of attack $\alpha \neq 0°$ its impact on the flow field could well be seen in the volume of rotor blade operation. Therefore, this contribution was also modeled in addition to the contributions of the main fuselage body.

The different test rigs are used for different rotor sizes, and to judge the relevance of individual fuselage shape characters on the flow field within the rotor disk the relative size and position of the volume of interest to the fuselage dimension is important to know. This is shown in Fig. 3 for all three fuselages.

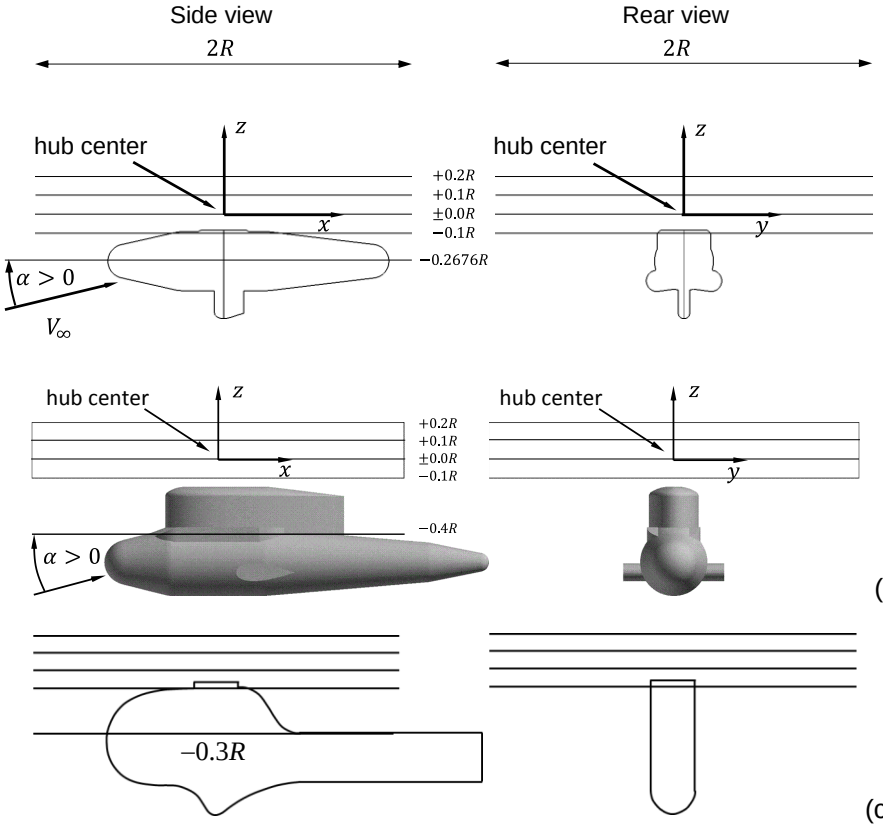

(a) LRTA, UH-60 size rotor

(b) RTA, Bo105 size rotor

(c) HART, model scale rotor

Fig. 3: Relative dimensions of the rotor blade operating volume with respect to the fuselage.

It is interesting to note that the lowest plane of data extraction, $z/R = -0.1$, is cut by the fuselage in case of the LRTA and HART, but not so in case of the RTA. Also, for the LRTA and HART there is some range where the fuselage surface is very close to the plane of data extraction and eventually large induced velocities will appear there.

In addition, these effects are located at small radial positions from the hub center, mainly within the blade root cutout where no airfoil can experience it, and up to a radial position of $0.3R$ any disturbances can be ignored anyway due to the extremely small dynamic pressure in these inner regions. All these effects are ignored in the parameter identification process later on since a blade attached to the hub center will never experience these, even when flapping downwards.

3. FUSELAGE-INDUCED VELOCITIES COMPUTED BY CFD

Fuselage-induced velocity fields of all three fuselages are presented next for three different angles of attack covering the range of LRTA and RTA attitudes. First, the lower extreme with $\alpha = -20°$ is shown in Fig. 4 for (a) the LRTA, (b) the RTA and (c) the HART fuselage. Since no data were available for HART at this angle of attack, they were interpolated linearly from data for $\alpha = -10°$ and $-30°$. In such a nose-down orientation the upwash in the front is quite strong. The usual sign convention is used here where downwash is positive and thus upwash is negative.

The peak values of upwash are close to $v_{izf}/V_\infty = -0.11$. Both LRTA and RTA indicate a very small magnitude of downwash downstream of the hub and right and left of the fuselage, while the centerline still indicates upwash. In contrast, the HART fuselage has a rather sharp curvature behind the hub that generates even in this nose-down condition a downwash of up to $v_{izf}/V_\infty = 0.03$. The sting support seems to be responsible for the upwash in the centerline at the downstream end of the data field at $x/R = 1$. In any case the asymptotic decay of the induced velocity profiles in both x and y directions are clearly visible. In addition, the HART fuselage generates the largest values both in upwash and in downwash; the RTA seems to have the smallest values, but differences to the LRTA are marginal.

The next set of data is given for a nose-up attitude of $\alpha = +10°$ in Fig. 5. In this case the downwash strength dominates the upwash, which is especially visible for the HART fuselage.

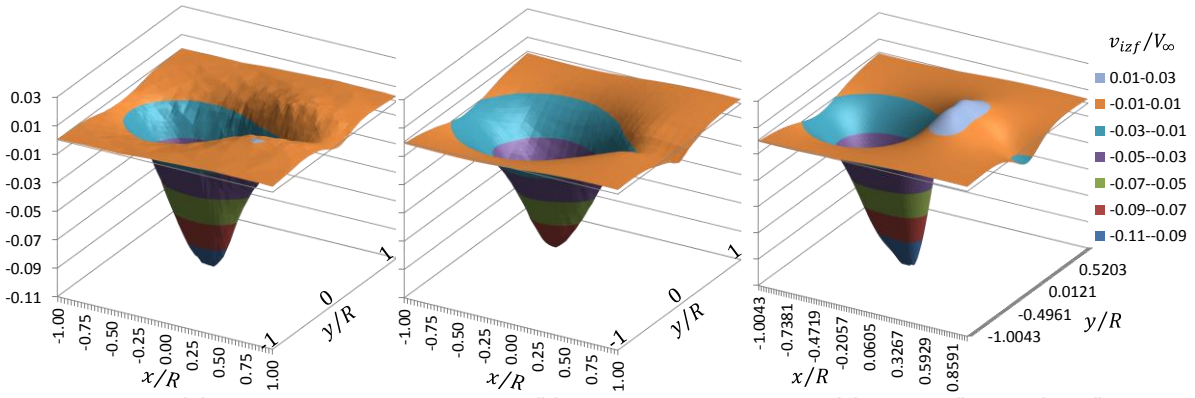

(a) LRTA (b) RTA (c) HART (interpolated)

Fig. 4: Fuselage-induced velocity distribution, $\alpha = -20°$, $z/R = 0.1$.

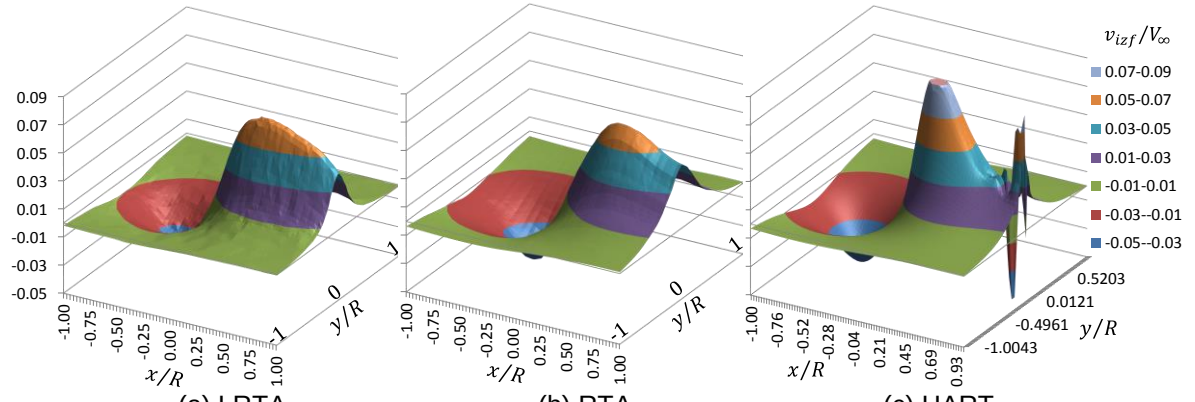

(a) LRTA (b) RTA (c) HART

Fig. 5: Fuselage-induced velocity distribution, $\alpha = +10°$, $z/R = 0.1$.

The large fuselage curvature aft of the hub generates a strong peak in downwash of $v_{izf}/V_\infty = 0.1$, which is much larger than that of the LRTA or RTA with $v_{izf}/V_\infty = 0.07$. However, this also causes flow separation to develop and to show up in the data of the HART fuselage at the downstream end of the figure around the centerline.

The spikes there are caused by small-scale local turbulence and are the instant image of an otherwise unsteady phenomenon that will occur periodically or stochastically, depending on the nature of flow separation. The goal of the model to be developed is not to simulate such unsteady effects. Its goal is to model the time-averaged mean velocity field. Therefore, such fluctuations need to be eliminated during the parameter identification process either by ignoring the error in these regimes or by significantly reducing it artificially.

In any case the fuselage-induced velocity distributions always show the asymptotic decay for increasing distance to the fuselage. The next will be to investigate the flow field behavior with increasing distance to the fuselage in the remaining z-direction. This is done for the RTA only, but is representative for the general behavior of all fuselages, and shown in Fig. 6. It can be seen from the different scales that the maximum upwash and downwash peaks of the fuselage-induced velocities reduce roughly by one half of the values with every increment away from the fuselage.

This is further demonstrated when plotting the peak values of upwash and downwash, as well as the peak-to-peak or $\Delta v_{izf}/V_\infty$ versus the distance from the hub center as is done in Fig. 7. The decay of upwash and downwash appears to be inversely to the distance from the fuselage center and asymptotically approaching zero for larger distances, which represents the expected potential theory behavior.

In terms of their extremes in upwash and downwash of fuselage-induced velocities the LRTA and RTA are quite similar to each other, while the HART fuselage generates larger peak velocities. This is due to larger curvatures of the HART fuselage in closer proximity to the rotor than in the other two cases. Also, the upwash in the front of the LRTA and the RTA fuselages is always larger than the downwash in the rear, while the HART fuselage generates upwash and downwash of comparable magnitude. Again, this behavior is caused by the fuselage shapes and especially their curvature. The general behavior, however, is quite the same for all three fuselages.

4. SEMI-EMPIRICAL MODEL OF FUSELAGE-INDUCED VELOCITIES

An in-depth description of the model is given in [5]. Physical considerations from potential theory require that all fuselage-induced velocities must die out for large distance to the fuselage. The magnitude is inversely reducing proportional to about the square of the distance to the center of the fuselage, as seen by the data Fig. 7 for the dependence on z/R and by the distributions shown in Fig. 4 to Fig. 6 for the dependence on x/R and y/R. In all angle of attack conditions shown, an upwash is found in the front region and a downwash in the rear region, their size and intensity depending on the angle of attack. Therefore, the hypothesis is made to make use of the superposition principle, i.e., to model the upwash and the downwash by separate functions and then adding their results. This suggests using a function such as

$$\frac{v_{izf}}{V_\infty} = \frac{A}{S_x\left(\frac{x-x_0}{R}\right)^2 + S_y\left(\frac{y-y_0}{R}\right)^2 + 1} \quad (1)$$

wherein A represents the peak value, S_x a decay factor for the profile of the fuselage-induced velocity distribution in x -direction, S_y respectively in y -direction, and x_0 is the peak position on the x-axis. Since in this specific setup without a side-slip angle the fuselage-induced velocities are symmetric in lateral direction (no side-slip) the respective y -coordinate of the peak value is zero: $y_0/R = 0$. Therefore, it can be eliminated from the formula. For each of the physical phenomena observed one formula of type Eq. (1) is applied and given subscripts u, d, t denoting the upwash, downwash and tail boom contributions.

The parameter identification is performed in three steps. First, every plane $z/R = const.$ for every angle of attack α is modeled fully independently from each other using Eq. (1). Therefore, the dependency of each of the four parameters A, S_x, S_y, x_0 for both the upwash function and the downwash function can be plotted versus z/R for each angle of attack (in total: 8 parameters for every of the 8 angles of attack times 4 planes $z/R = 8 \cdot 8 \cdot 4 = 256$ parameters). It is found that in general they show a dependency as shown in Fig. 7 while the peak position x_0 found is essentially independent on z/R. The magnitude and the decay factors all are dependent on the distance to the fuselage, such that they may be modeled in the form

$$A = \frac{A_0}{S_{A0}\left(\frac{z-z_0}{R}\right)^2 + 1}$$

$$S_x = \frac{S_{x0}}{\left(\frac{z-z_0}{R}\right)^2}; \quad S_y = \frac{S_{y0}}{\left(\frac{z-z_0}{R}\right)^2} \quad (2)$$

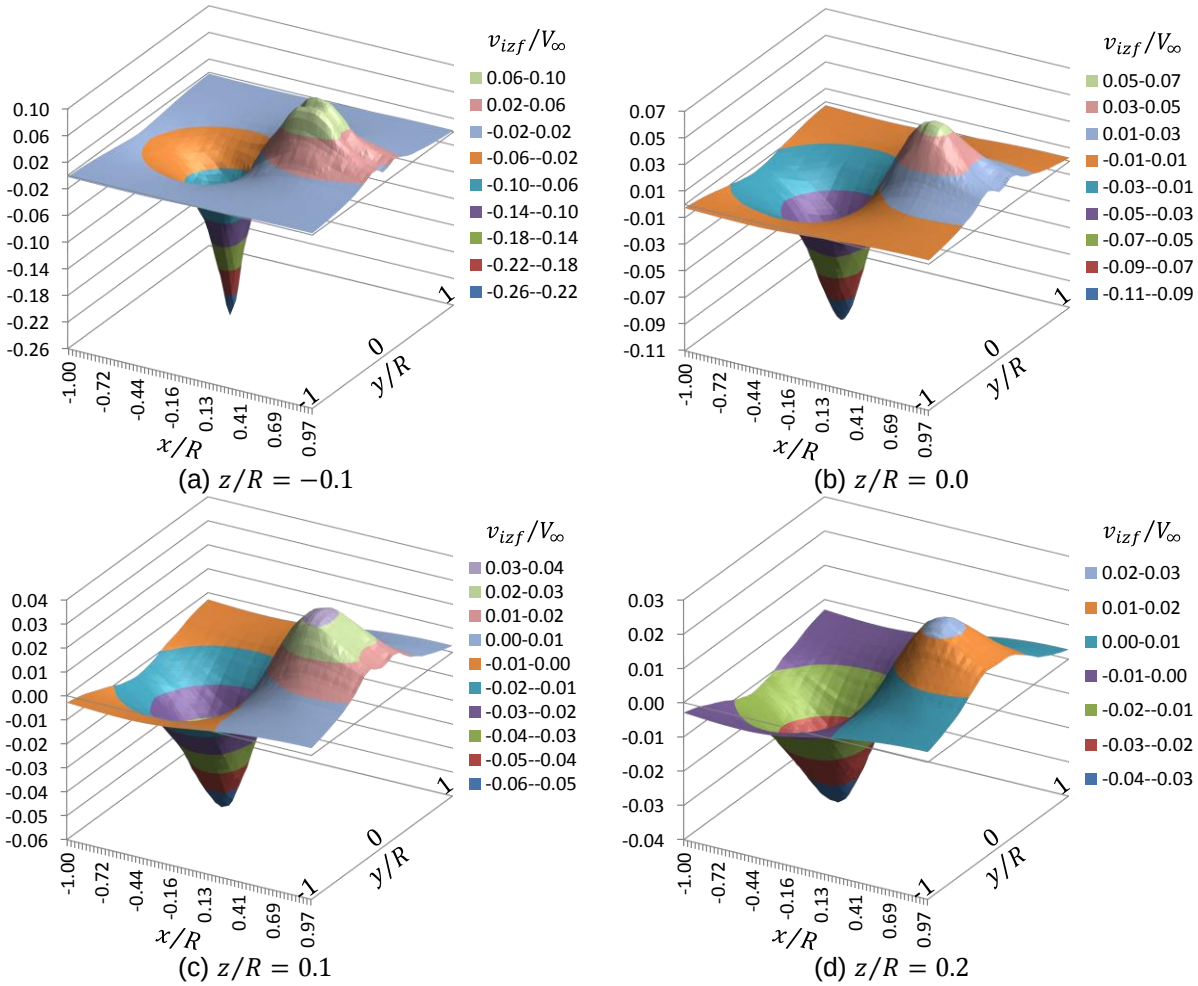

Fig. 6: Influence of z/R on fuselage-induced velocity distribution, RTA, $\alpha = 0°$.

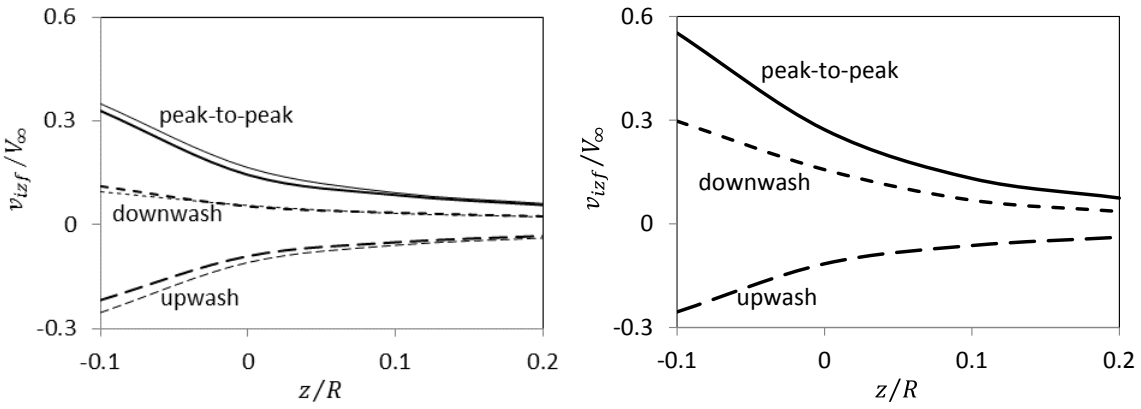

Fig. 7: Peak fuselage-induced velocities' dependence on z/R, $\alpha = 0°$.

Therein, S_{A0} represents the respective decay factor for the variation of A in z-direction, with A_0 as the amplitude at $z = z_0$ and z_0 is the position of the maximum of A on the z-axis, which is considered the center of the fuselage, measured from the hub center as the reference coordinate system. The reason for doing so is found in potential theory: the distribution of sources and sinks to generate a contour of these fuselage bodies will be placed on their respective centerline. By intention S_x, S_y become infinite at $z = z_0$, which allows a smooth variation from upwash on the upper side of the fuselage to downwash on the lower side because then the fuselage-induced velocity becomes zero at $z = z_0$ to avoid a singularity. While the LRTA and RTA model are sufficiently represented by the upwash and downwash function,

the HART has a stronger influence of the tail boom support and accordingly a third function of the type as given by Eq. (1) is added to represent this effect.

The second step of parameter identification is to combine Eqs. (1) and (2) in order to achieve an analytical representation for the entire (x,y,z)-domain. This adds one parameter for each upwash and downwsh function to a total of 10 parameters for each of the 8 angles of attack (reducing the total number to $10 \cdot 8 = 80$ parameters). All those parameters are then plotted versus the angle of attack to identify this last dependency. The angle of attack has been made non-dimensional through division by $90°$, such that in the extreme angles of $\alpha = \pm 90°$ (HART data are available up to these) the non-dimensional values become -1 and $+1$. It is found that most of the parameters are essentially linear or quadratic in α within the range $-20° \le \alpha \le +15°$, such that the following relations can be used to approximate them (LRTA and RTA; either α or $\alpha/90°$ may be used therein).

$$
\begin{aligned}
A_0 &= A_{00} + A_{01}\alpha + A_{02}\alpha^2 \\
S_{A0} &= S_{A00} + S_{A01}\alpha \\
S_{y0} &= S_{y00} + S_{y01}\alpha + S_{y02}\alpha^2 \\
S_{x0} &= S_{x00} + S_{x01}\alpha \\
x_0 &= x_{00} + x_{01}\alpha
\end{aligned}
\qquad (3)
$$

The third and final step of parameter identification is thus to identify these additional parameters, wherein A_{00} is the magnitude for $\alpha = 0°$, A_{01} the variation linear proportional to α and A_{02} the variation proportional to the square of α, etc., as given in Eq. (3). Similarly, x_{00} is the peak position for $\alpha = 0°$, x_{01} the variation linear proportional to α. In total, only 22 parameters are resulting that all have a physical interpretation.

Now the entire flow field within the volume of the data given ($-1 \le x/R \le +1, -1 \le y/R \le +1, -0.1 \le z/R \le +0.2$) can be analytically represented by the math model for all angles of attack $-20° \le \alpha \le +15°$ and any in between. The x-position of the tail boom function used only in the HART model, however, is fixed to $x_t/R = +1$ since it is extending also aft of the rotor. A sufficient degree of accuracy if in average is obtained, if the error relative to the peak-to-peak data range within each individual plane is less equal 5%. This goal is achieved as seen in Fig. 8, where the mean relative error is shown after the first step of parameter identification, and in Fig. 9 of the final model after step 3.

The smallest errors are obtained in step 1 since this allows the largest degree of freedom with one parameter set for each individual plane z/R. Step 3 combines all dependencies on x,y,z and α in one fully analytical model with a few parameters only, thus increasing the overall error. However, it is still below the goal of 5% relative error.

Also, due to the nature of the functions used, see Eqs. (1) and (2), the fuselage-induced velocities asymptotically approach zero for $(x,y,z)/R \to \pm\infty$ as required by potential theory. Therefore, the model can also be used outside of the volume of data it is based on. If it is desired to also compute approximately the fuselage-induced velocities below the fuselage – although no data are extracted to build up a separate model for this region – the following consideration can be applied. Due to the approximate symmetry of the fuselage body with respect to the plane z_0/R the flow field below it can be assumed to be

$$
\frac{v_{izf}}{V_\infty}(\alpha, z < z_0) = -\frac{v_{izf}}{V_\infty}(-\alpha, z > z_0) \qquad (4)
$$

The CFD data of the HART fuselage cover a much wider range of angle of attack $-90° \le \alpha \le +90°$ for no side-slip, $\beta = 0°$, and also for the range of side-slip angles $0° \le \beta \le +90°$ for no angle of attack, $\alpha = 0°$. The behavior of the parameters with respect to α thus is much more non-linear; as representative example the factors influencing the shape in x and y-direction are given in Fig. 10.

The position of the upwash and downwash extremes is found to vary about linearly with angle of attack. Most of the other parameter's dependencies with respect to α show an asymptotic behavior for large angles with a continuous variation between them. This behavior can be described by two generic functions, where X is a placeholder for the parameter symbols.

$$
X^- = X_0\left[\frac{1}{X_1(1-\alpha/90)^6+1} - \frac{1}{X_1+1}\right]
$$

$$
\text{or} \quad X^+ = X_0\left[\frac{1}{X_1(1+\alpha/90)^6+1} - \frac{1}{X_1+1}\right] \qquad (5)
$$

$$
\text{with} \quad X = A_0,\ S_{A0},\ S_{x0},\ S_{y0}
$$

$$
x_0 = x_{00} + x_{01}\alpha
$$

The exponent therein is empirical and gives best fit to the curves found here. This is applied to all the parameters of the upwash, downwash and tail boom functions, except for $x_t/R = 1$ as mentioned before and for the magnitude, which is modeled by a Sine function.

$$
A_{0t} = A_{00t} + A_{01t}\sin\alpha \qquad (6)
$$

The side-slip conditions were computed for the HART fuselage only and the procedure of parameter

identification is the same as for the angle of attack. Note that in side-slip conditions the tail boom-induced velocity field is represented by two functions, where one of them is part of the modeling in α and the second one is only present for $\beta \neq 0$. The reason is that when a pure angle of attack is present the tail boom generates only upwash or only downwash above it, depending on the sign of α.

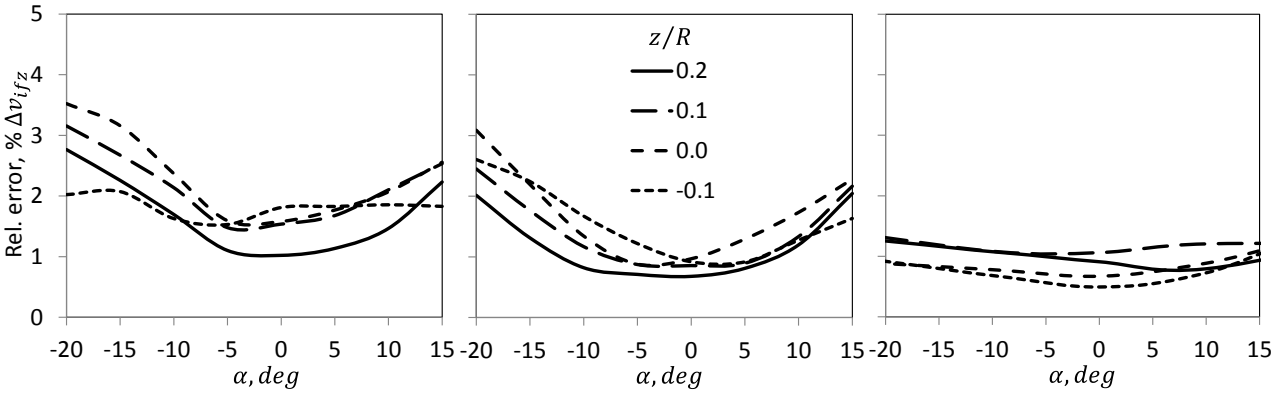

(a) LRTA (b) RTA (c) HART

Fig. 8: Mean relative error after step 1 of parameter identification.

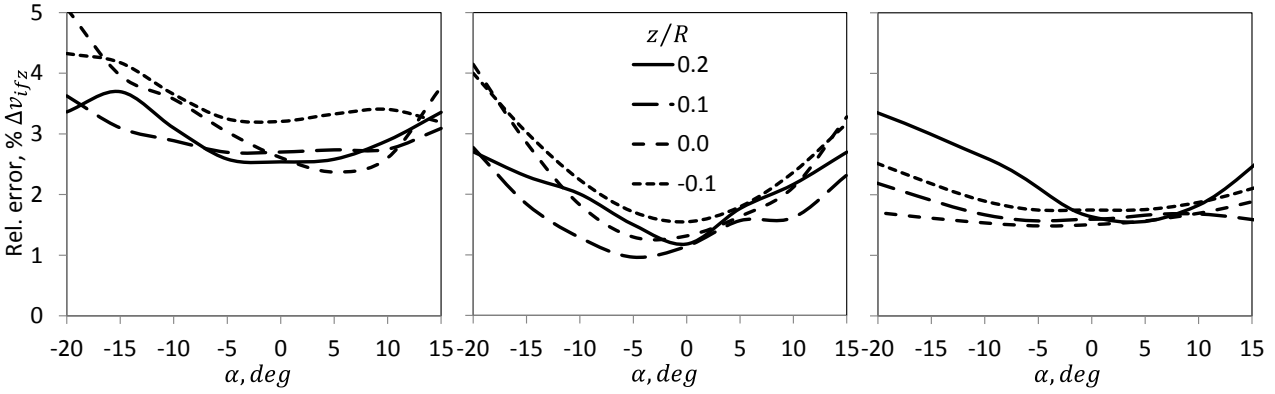

(a) LRTA (b) RTA (c) HART

Fig. 9: Mean relative error after step 3 of parameter identification.

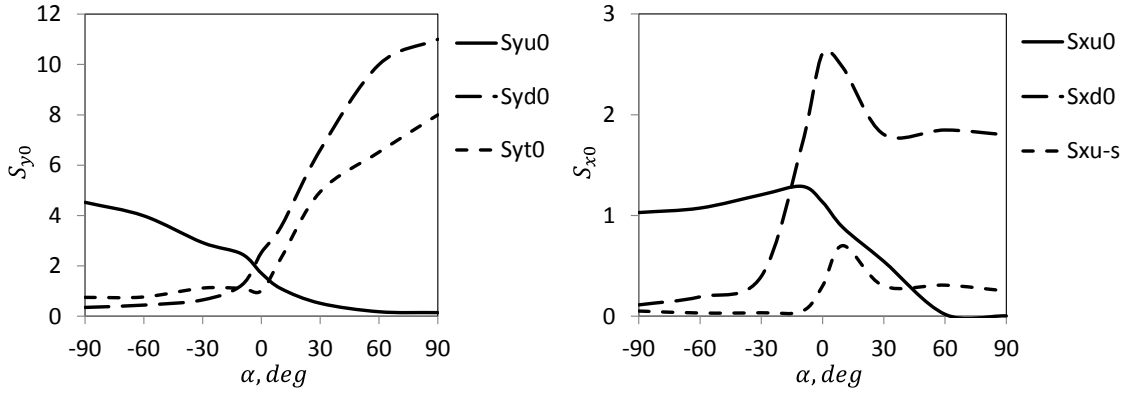

(a) Shape factor, y (b) Shape factor, x

Fig. 10: Dependence of shape factors on $\alpha; \beta = 0°$.

In side-slip, the tail boom generates an upwash on the windward side and a downwash on the leeward side, such that one function of the type of Eq. (1) is needed for each of these. When plotting the results of step 2 of the parameter identification versus the side-slip angle β in the same way as done in Fig. 10 for α, it appears that all parameters identified within step 2 vary essentially proportional either to $\sin|\beta|$ or to $1 - \cos\beta$.

$$X^s = X_0 + X_1 \sin|\beta| \quad \text{or} \quad X^c = X_0 + X_1(1-\cos\beta) \quad \text{with} \quad X = A_0,\ S_{A0},\ S_{x0},\ S_{y0},\ x_0,\ y_0 \tag{7}$$

In side-slip all the upwash areas move to the windward side and all the downwash areas to the leeward side, therefore the function centers also move towards these sides and $y_0 \neq 0$ in Eq. (1). Step 3 of both the angle of attack range formulation and of the side-slip angle formulation is set up in a way such that the model for $\alpha = \beta = 0°$ is the same in both and all variations of this basic model due to α and β are superimposed to it. In addition, any combinations of α and β – though not supported by CFD data – should be possible to predict in a meaningful way as well. This is achieved by a proper blending function using f_α and f_β as given in Eq. (8), which leads to a continuous variation from pure α to pure β. However, this blending is purely empirical and needs verification by CFD computation for some combined α, β conditions.

The accuracies achievable in this large range of angles including partly massive flow separation is of course worse than in the small angle of attack range. The separated flow regimes needed to be ignored during the parameter identification in a proper way, and of course are ignored in the error computation as well. The error thus refers only to the areas of clean undisturbed flow. Nevertheless, it was possible to remain essentially with an accuracy of 6% of the peak-to-peak data range within each plane z/R as shown in Fig. 11.

$$\frac{v_{izf}}{V_\infty}(\alpha,\beta) = \frac{v_{izf}}{V_\infty}(\alpha=\beta=0°) + \frac{\Delta v_{izf}}{V_\infty}(\alpha,\beta=0°)\, f_\alpha + \frac{\Delta v_{izf}}{V_\infty}(\alpha=0°,\beta)\, f_\beta$$
$$f_\alpha = 1 - f_\beta \qquad f_\beta = \cos\alpha \frac{|\beta|}{|\alpha| + |\beta| + 0.0001} \tag{8}$$

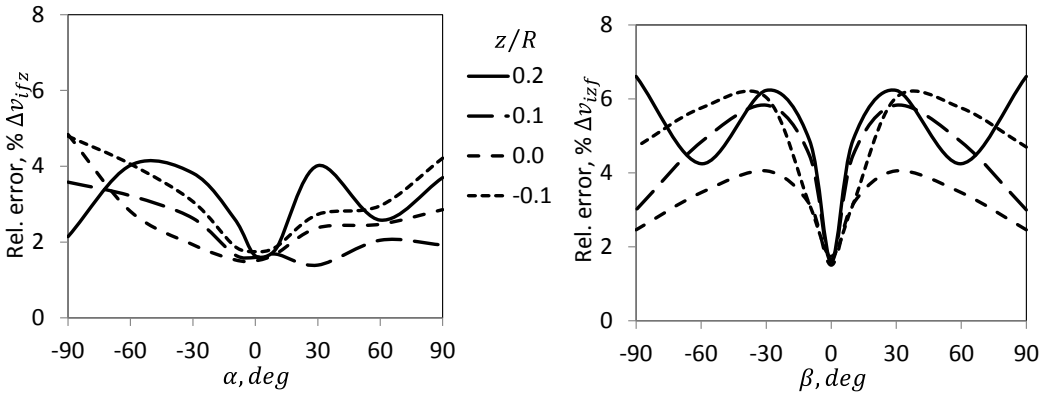

(a) α-variation (b) β-variation

Fig. 11: Mean relative error after step 3 of parameter identification.

5. COMPARISON: MODEL VERSUS CFD DATA

A sample result is given in Fig. 12, comparing the CFD-generated data on the left with data reconstruction using the math model developed to the right; the wind is always from the left. The angle of attack is zero common for all fuselages, showing the individual differences due to the fuselage shapes and also that the model is able to adapt to these specifies in a plane $z/R = 0.1$ above the hub center. Note the different peak values of upwash in the front and downwash in the rear, as well as the slightly different shapes. The large circles indicate the rotor radius and the contour inside represent the specific fuselage of the LRTA, RTA and HART. Also note that the scale range for the fuselage-induced velocities in case of HART is larger than for the LRTA and RTA.

It is obvious that the model is able to reconstruct the CFD data to a high degree of accuracy sufficient at least for use in comprehensive rotor codes. The mean values, and especially the magnitude and shape of inflow variations experienced at the revolving rotor blades can therefore be taken into account in a proper, easy and reliable way. More data are given in the Appendix for angles of attack of $\alpha = -20°$ in Fig. 21 and for $+10°$ in Fig. 22.

For the HART fuselage, extremes in angle of attack $\alpha = \pm 90°$ are also of interest and shown in Fig. 13. Again, the essential features of the CFD data are well represented by the model. In case of hover or vertical climb, $\alpha = -90°$ shown in Fig. 13 (a), the fuselage is blown from top and the rotor operates in clean flow, partly blocked by the fuselage especially

in the center. To the right the tail boom blockage is well visible and also represented by the model in size and intensity. In vertical descent, $\alpha = +90°$ shown in (b), the fuselage is blown from bottom upwards and thus upon it separated flow and associated turbulence is found in the CFD data that passes through the entire volume of rotor operation, but is confined to the centerline. The model can only represent the mean flow features without these turbulent separated structures, but the magnitude and distribution indicate this is achieved sufficiently well.

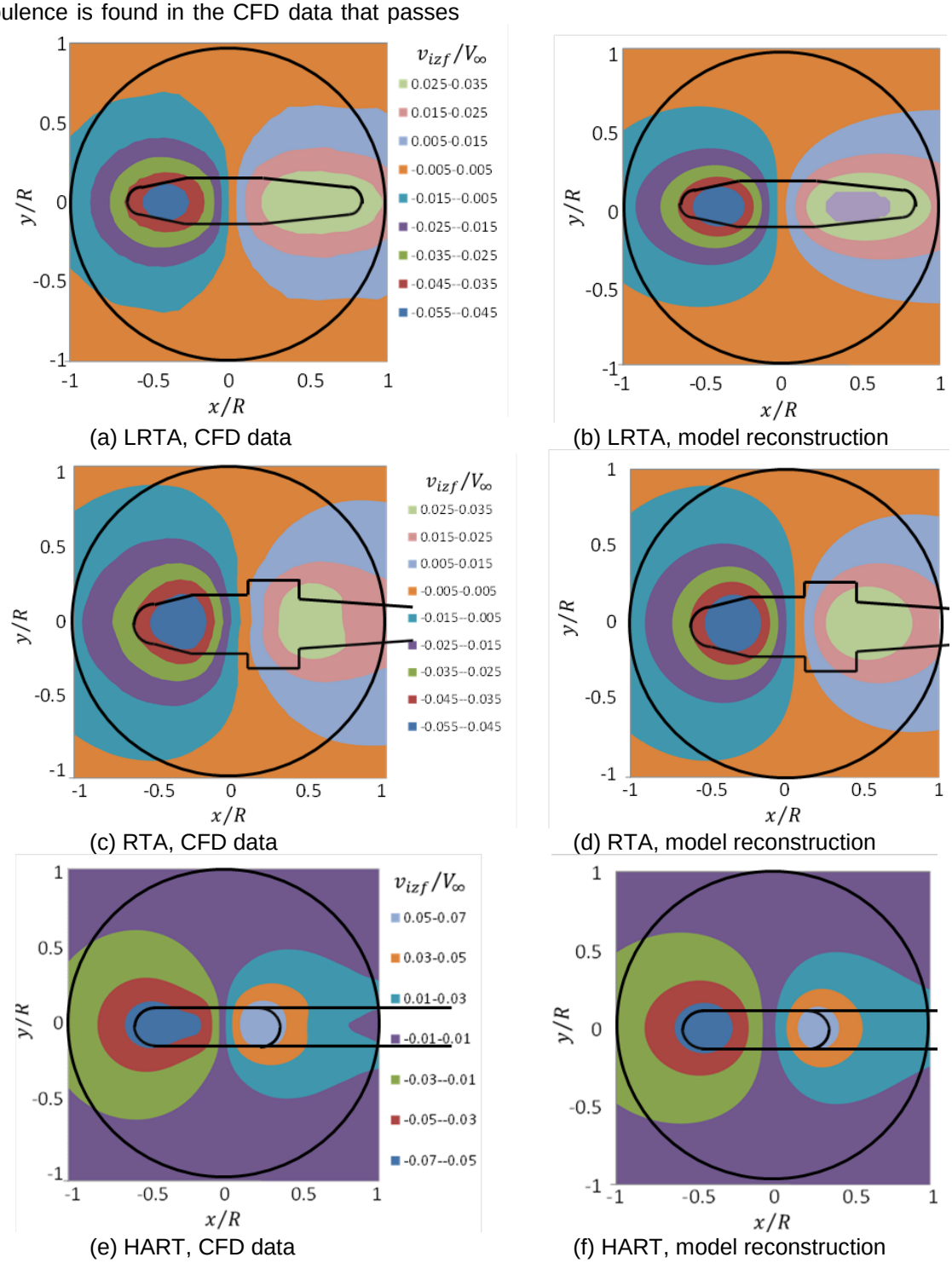

(a) LRTA, CFD data

(b) LRTA, model reconstruction

(c) RTA, CFD data

(d) RTA, model reconstruction

(e) HART, CFD data

(f) HART, model reconstruction

Fig. 12. Comparison of CFD data with the model. $\alpha = 0°, z/R = 0.1$, wind from left.

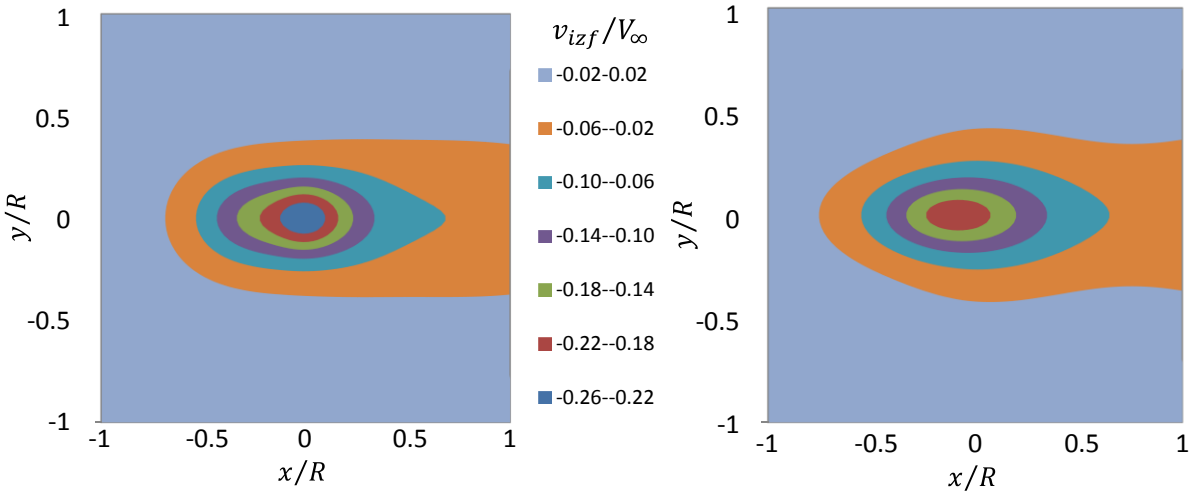

(a) $\alpha = -90°$: CFD data (left), model (right); wind from top.

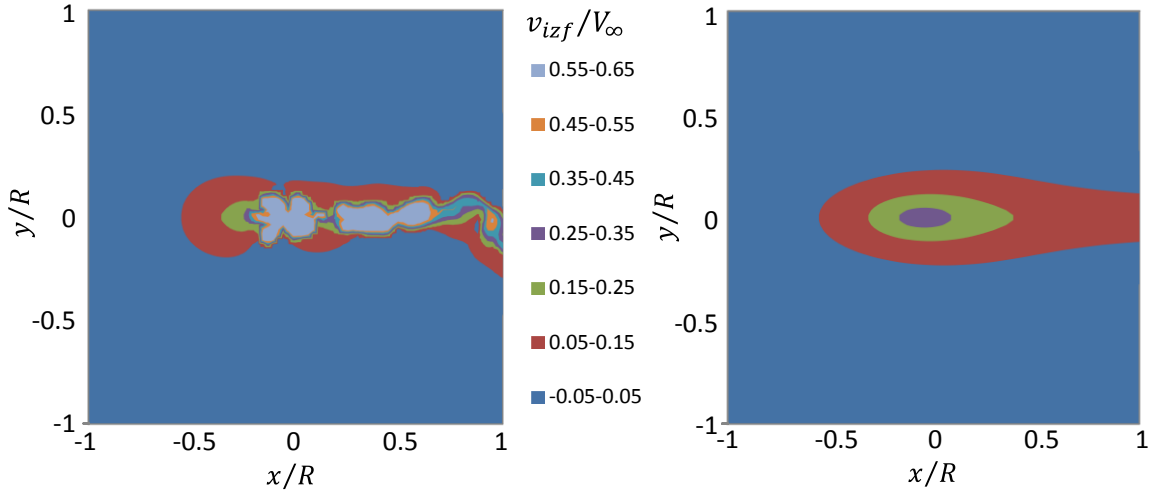

(b) $\alpha = +90°$: CFD data (left), model (right); wind from bottom.

Fig. 13. Comparison of CFD data with the model for extreme angles of attack, HART, $z/R = 0.1$.

Finally, the side-slip conditions are of interest. These are given in Fig. 14 for $\beta = 10°, 30°, 90°$. Again, the model performs well in representing the important features of the CFD data. Due to the symmetry of the fuselage, negative angles need not be modeled separately; the flow field only needs to be mirrored at $y/R = 0$: $v_{izf}(x, y, z, -\beta) = v_{izf}(x, -y, z, \beta)$. For $\beta = 10°$ no flow separation takes place, this begins at $\beta = 30°$ and progressively increases in intensity and space covered towards $\beta = 90°$, especially in the lowest plane $z/R = -0.1$. The model, of course, cannot represent these separated flow turbulent structures and only the estimated mean (as if time averaged) values are represented. The maximum upwash peak on the windward side is found much closer to the fuselage centerline than the downwash peak on the leeward side which appears at a much larger lateral distance to the fuselage. Also, the variation of the x-position of the peak is matched well. Finally, the tail boom effect shows up in an extension of the upwash on the windward side to the rear end of the graphs for $\beta \geq 30°$. The associated impact on the downwash is more visible for smaller side-slip angles $\beta \leq 30°$, but is still present for larger ones. However, it is hidden in the larger scale range of fuselage-induced velocities at large side-slip angles.

6. EFFECT OF FUSELAGE-ROTOR INTERFERENCE ON ROTOR TRIM

Analytic results can be obtained from simple blade element theory assuming constant inflow, linear steady incompressible 2D aerodynamics, no flapping motion, and centrally hinged blades trimmed for zero hub moments [5]. Results shown in the following are for a given thrust coefficient of $C_T = C_W = 0.00484$ with the rotor solidity assumed as $\sigma = 0.07$, which is representative for a 2.2 ton Bo105 helicopter. Analytical results require a polar coordinate representation of the fuselage-induced velocity field, which so far is formulated in Cartesian coordinates, see Eqs. (1) and (2).

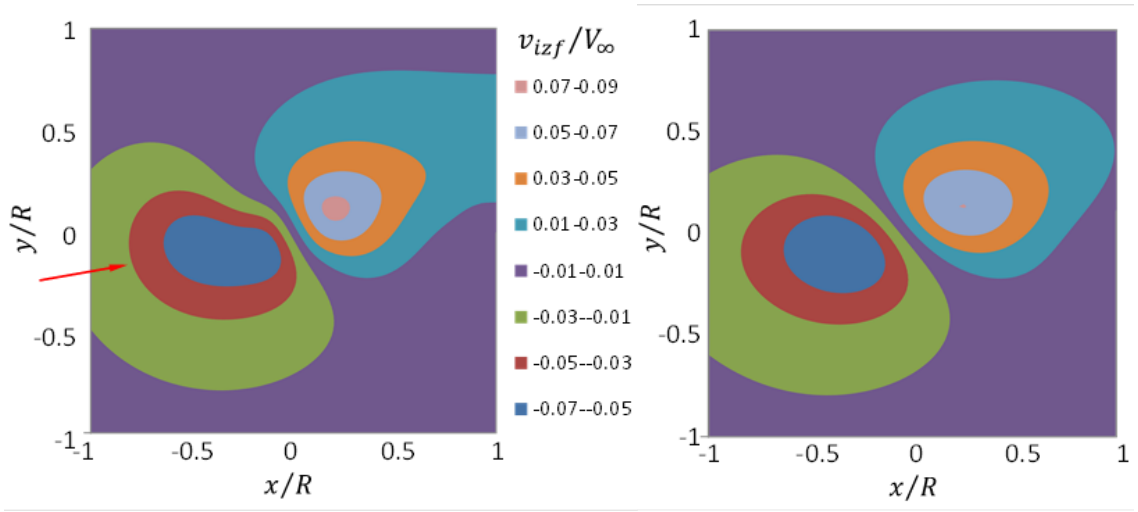

(a) $\beta = 10°$: CFD data (left), model (right)

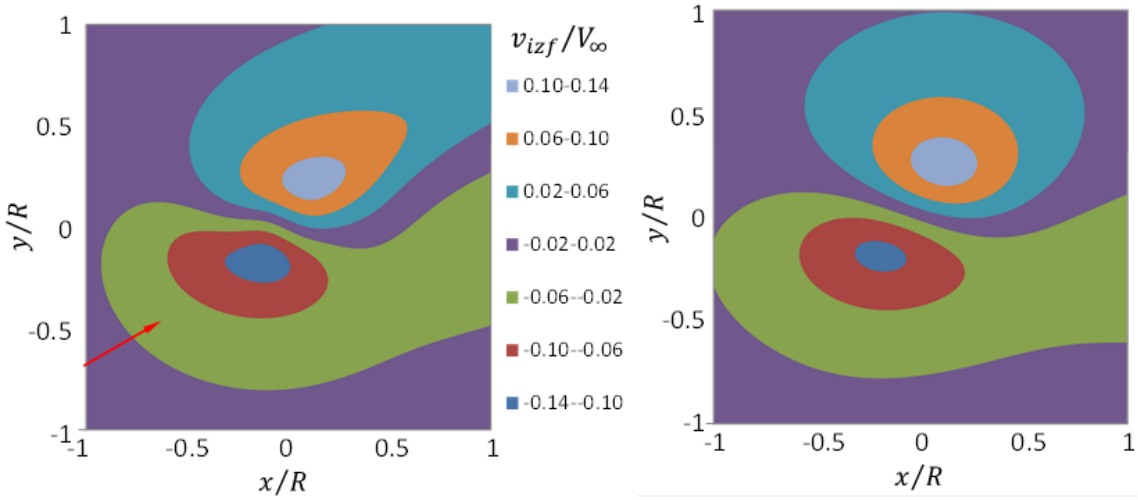

(b) $\beta = 30°$: CFD data (left), model (right)

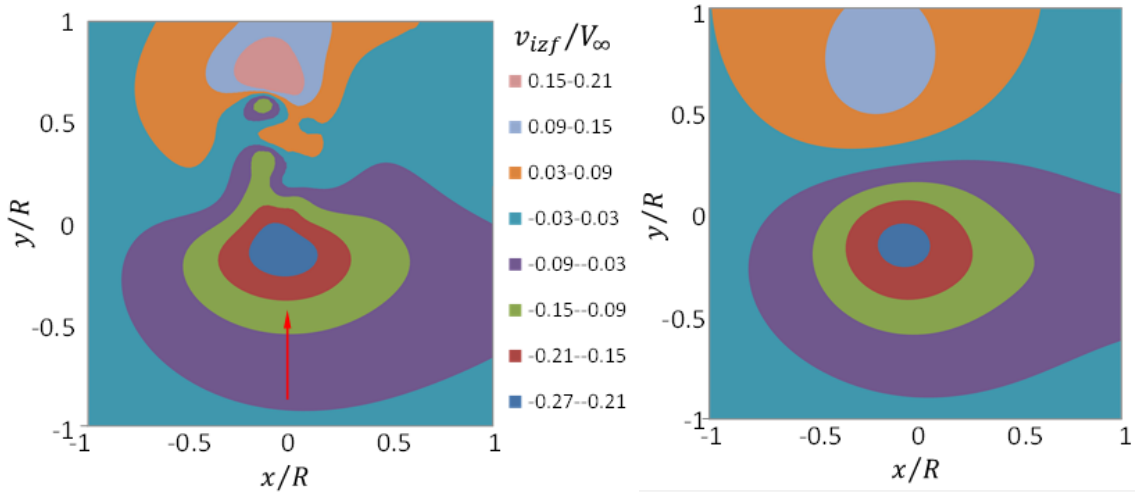

(c) $\beta = 90°$: CFD data (left), model (right)

Fig. 14. Comparison of CFD data with the model for side-slip angles, HART, $z/R = 0.1$.

For this, the model is evaluated at equidistant radial and azimuthal positions first, then for each radial position a Fourier analysis is performed and finally the Fourier coefficients dependence on the radial coordinate are approximated by a polynomial of third order ($J = 3$).

Due to the lateral symmetry of the flow field in pure angle of attack settings only Cosine terms result; in case of side-slip angles both Cosine and Sine terms will show up until in quartering flight $\beta = \pm 90°$ the Sine terms will dominate the result, but the Cosine will not be zero since the front part of the fuselage is different to the rear part, which causes a non-symmetry of the flow field with respect to the plane $x/R = 0$. Considering pure α variations, the fuselage-induced inflow, referenced to the tip speed, can be written as given in Eq. (9) (for a given α and a fixed value of z/R):

$$\frac{v_{izf}(r,\psi)}{V_\infty} = \sum_{n=0}^{\infty} \lambda_{izfn}(r)\cos(n\psi) \qquad \lambda_{izfn}(r) = \sum_{j=0}^{J} c_{nj} r^j \tag{9}$$

Using blade element velocities tangential to the rotor disk V_T and perpendicular to it V_P to compute the local dynamic pressure (simplified as $V_T^2\,\rho/2$), and the blade element angle of attack α_a from Eq. (10)

$$\begin{aligned} V_T &= \Omega R(r + \mu\sin\psi) \\ V_P &= \Omega R \mu \lambda_{izf}(r,\psi) \\ \alpha_a &= \Theta - \arctan(V_P/V_T) \\ &\approx \Theta_C\cos\psi + \Theta_S\sin\psi - V_P/V_T \end{aligned} \tag{10}$$

an expression for the thrust increase or decrease due to the fuselage-induced inflow can be derived, which is given in Eq. (11) (A and B are the effective non-dimensional radii of the beginning and the end of the airfoiled section of the blade, the approximation makes use of $A = 0, B = 1$)

$$\begin{aligned} \frac{\Delta C_T}{C_W} &= \frac{1}{2\pi}\int_0^{2\pi}\int_A^B \frac{dC_T}{C_W} d\psi \\ &= \mu\frac{\sigma\pi}{C_W}\left(\Delta\Theta_S\,\frac{B^2 - A^2}{2} - \sum_{j=0}^{J} c_{0j}\,\frac{B^{j+2} - A^{j+2}}{j+2}\right)\left(\frac{\pi}{2} - \theta\right) \approx \mu\frac{\sigma\pi}{C_W}\left(\frac{\Delta\Theta_S}{2} - \sum_{j=0}^{J}\frac{c_{0j}}{j+2}\right) \end{aligned} \tag{11}$$

The cyclic controls required to keep hub moments the same as for the isolated rotor results are given in Eq. (12) (the approximations again are obtained using $A = 0, B = 1$):

$$\begin{aligned} \Delta\Theta_C &= \mu\frac{\sum_{j=0}^{J} c_{1j}\,\frac{B^{j+3} - A^{j+3}}{j+3}}{\frac{B^4 - A^4}{4} + \mu^2\frac{B^2 - A^2}{8}} \\ &\approx \frac{8\mu}{2+\mu^2}\sum_{j=0}^{J}\frac{c_{1j}}{j+3} \\ \Delta\Theta_S &= \mu^2\frac{\sum_{j=0}^{J}\left(c_{0j} - \frac{c_{2j}}{2}\right)\frac{B^{j+2} - A^{j+2}}{j+2}}{\frac{B^4 - A^4}{4} + 3\mu^2\frac{B^2 - A^2}{8}} \\ &\approx \frac{4\mu^2}{2+3\mu^2}\sum_{j=0}^{J}\frac{2c_{0j} - c_{2j}}{j+2} \end{aligned} \tag{12}$$

As can be seen from these analytical results, the fuselage impact on thrust requires the radial distribution of the steady part of fuselage-induced flow (expressed by c_{0j} in Eq. (11)) and also the change in longitudinal control $\Delta\Theta_S$. This, in reverse, requires the steady and the 2/rev part in $2c_{0j} - c_{2j}$, see Eq. (12). The change in lateral control $\Delta\Theta_C$ only depends on the 1/rev part of the fuselage flow field, c_{1j}. The change in thrust and lateral cyclic due to the fuselage appears widely linear in the advance ratio μ, since they are affected by the upwash in the front and the downwash in the rear. In contrast, the longitudinal control is affected by μ^2 due to the asymmetry of dynamic pressure on the advancing and retreating side. However, physical consideration already suggests that the $\Delta\Theta_S$ will be very small compared to $\Delta\Theta_C$ due to lateral symmetry of the fuselage-induced flow field when $\beta = 0°$.

The evaluation of the coefficients of the fuselage-induced flow field c_{nj} can be done for different angle of attack α and for different separation distances z/R of the rotor to the fuselage to investigate the individual effects. In the following the effect of α is shown at a representative rotor position of $z/R = 0.05$.

The change in thrust as estimated by simple blade element/momentum theory exemplarily is shown next in Fig. 15 for a rotor of UH-60 size on the LRTA, a rotor of Bo105 size on the RTA, and a model scale sized rotor on the HART test rig for the range of attitudes in wind tunnel operation. Following Eq. (11) the mean part of the fuselage-induced velocities is the dominant contribution to the rotor thrust. Nose-down attitudes cause the generation of more upwash than downwash, thus the thrust is increasing and vice versa, the effect grows proportional to wind speed, and the magnitude is depending on rotor size relative to the fuselage dimensions as well as to the vertical separation of the hub from the fuselage. Depending on the shape of the fuse-

lage the changes in thrust can reach from -4% to $+5\%$ of the helicopter weight (LRTA, HART) and even 10% in case of the RTA at the highest advance ratio, but for angles of attack $\alpha \approx 0°$ the fuselage effect is negligible.

Fig. 16 shows the major fuselage impact on rotor trim, namely on the lateral control angle. The strong variation of upwash in the front and downwash in the rear represents a 1/rev Cosine variation in blade element angle of attack and thus needs a 1/rev lateral control angle in order to compensate the fuselage-induced flow field to maintain trim, as given by Eq. (12). The radial location of the maximum induced velocities plays a role here, in addition to its magnitude. The smallest impact is found for the LRTA, while the RTA and the HART are quite similar. Nose-up attitudes generate a larger increase in downwash than the upwash is reduced, thus a larger 1/rev variation and consequently a larger lateral control to compensate this. For nose-down attitudes this is opposite and less control is needed.

The longitudinal control is much less affected than the lateral control due to the lateral symmetry of the fuselage-induced flow field in forward flight. It depends on the mean and the 2/rev part of the flow field, see Eq. (12). As can be seen from Fig. 17 the changes in control needed to retrim the rotor are about one magnitude smaller than the lateral control shown before. The potential induced flow field outside the fuselage asymptotically approaches zero for large distances to it. It is of interest, how large a distance between fuselage and rotor hub need to be in order to have negligible influence of the fuselage. In the following the effect of the rotor's distance to the fuselage is investigated for a separation up to two radii away from it, all following figures are for an advance ratio of $\mu = 0.5$ where the largest impact on rotor trim was found so far. The fuselage impact on rotor thrust is indeed asymptotically decreasing as seen in Fig. 18.

At a distance of two radii the maximum change of thrust is about 1% for either extremes of angle of attack, and practically zero for $\alpha = 0°$. As in case of ground effect about three rotor radii are sufficient to ignore fuselage effects on rotor thrust.

This is even more pronounced when looking at the lateral control in Fig. 19. For half a radius distance to the fuselage the change in control has already shrunk to about $0.2°$, from $1.2°$ at the regular hub position. For $z/R = 2$ the changes in lateral control are far below $0.1°$ and negligible, which is similar to a rotor in ground effect, where $3R$ distance are considered as the limit of being out of ground. The longitudinal control angle was much less affected by the presence of the fuselage than the lateral control as sown before. An increasing distance to the fuselage further reduces this effect as shown in Fig. 20 (note the smaller scale compared to Fig. 19). Again, two rotor radii will result in control angle changes of significantly less than $0.1°$ and thus negligible effects.

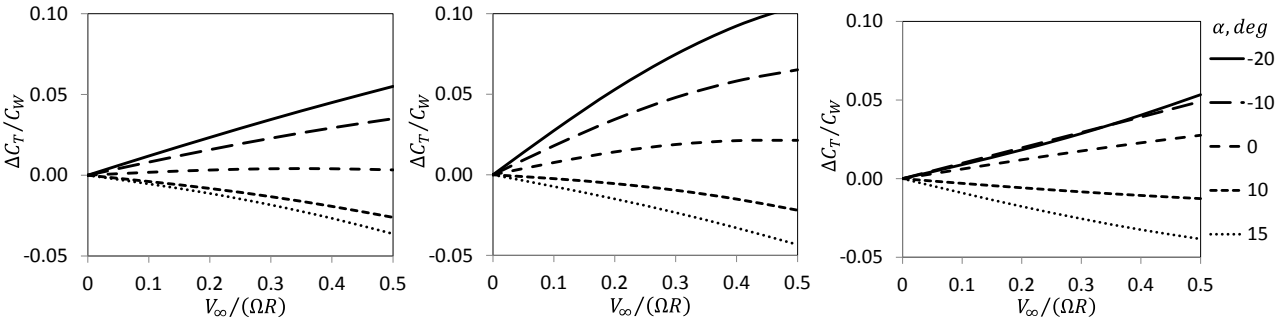

(a) LRTA (b) RTA (c) HART

Fig. 15. Prediction of fuselage-induced velocities on change of rotor thrust, $z/R = 0.05$.

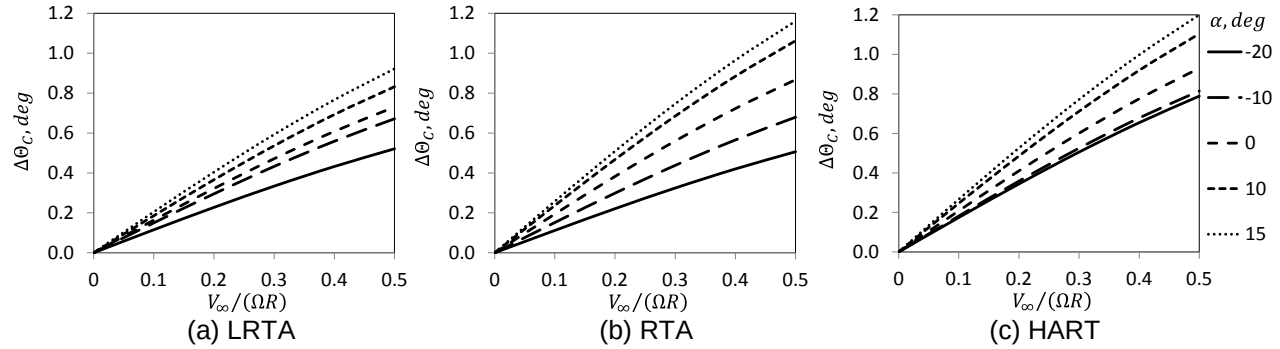

(a) LRTA (b) RTA (c) HART

Fig. 16. Prediction of fuselage-induced velocities on change of lateral control, $z/R = 0.05$.

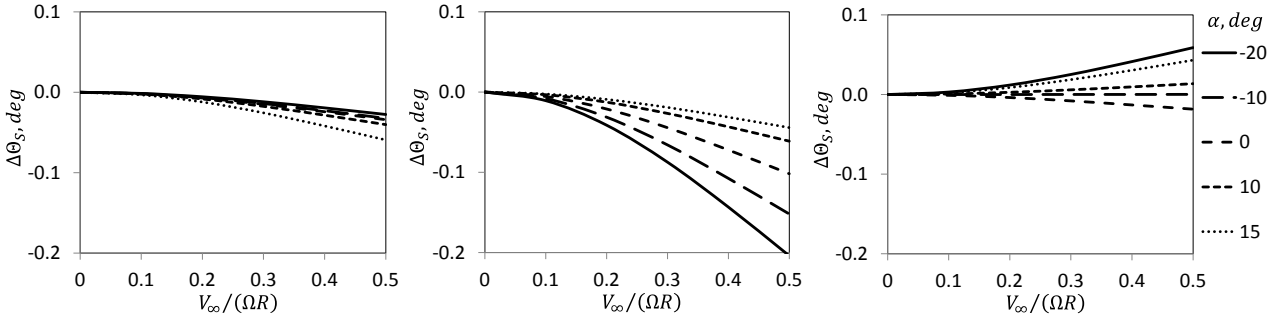

(a) LRTA (b) RTA (c) HART

Fig. 17. Prediction of fuselage-induced velocities on change of longitudinal control, $z/R = 0.05$.

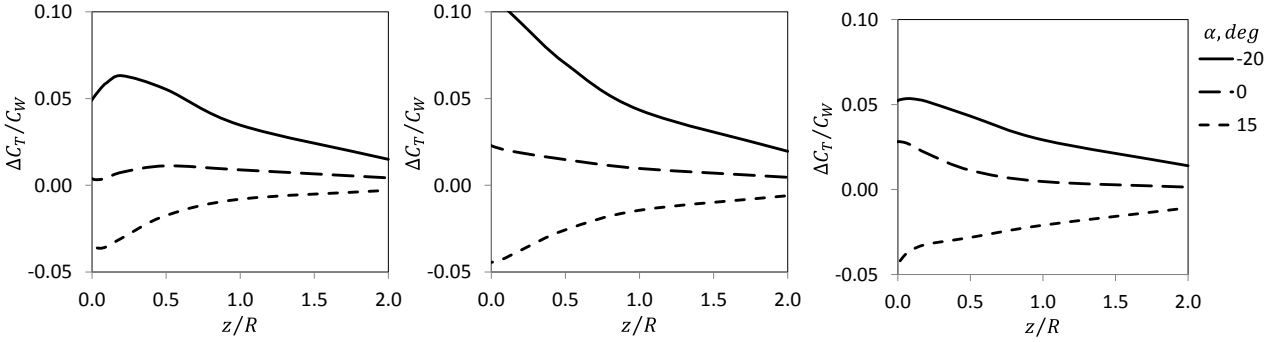

(a) LRTA (b) RTA (c) HART

Fig. 18. Prediction of fuselage-rotor separation on change of rotor thrust, $\mu = 0.5$.

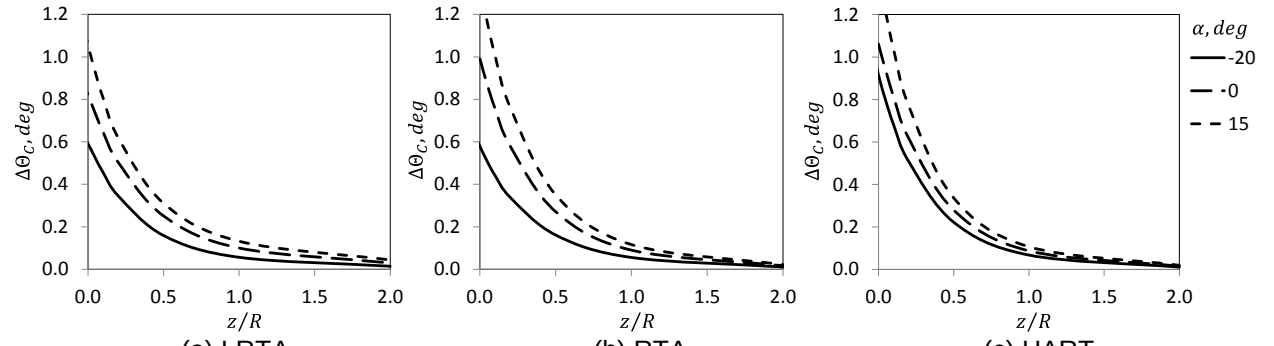

(a) LRTA (b) RTA (c) HART

Fig. 19. Prediction of fuselage-rotor separation on change of lateral control, $\mu = 0.5$.

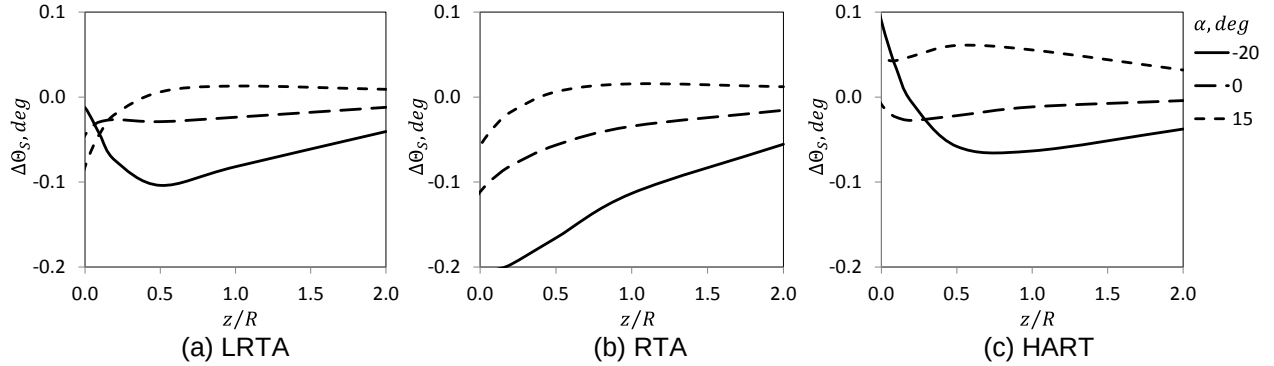

(a) LRTA (b) RTA (c) HART

Fig. 20. Prediction of fuselage-rotor separation on change of longitudinal control, $\mu = 0$.

7. CONCLUSIONS

It is shown that the nonlinear fuselage-induced flow field can be reconstructed by a simple analytical model with good accuracy (an average error less than 5% of the peak-to-peak data range within the volume of rotor blade operation for the entire range of angle of attack), which is deemed sufficient for helicopter comprehensive code environments. Individual characteristics of fuselage shapes can correctly be represented by the model and it can easily

be extended to include the effects of further components like tail booms, horizontal stabilizers, wings, etc. This allows the inclusion of fuselage-rotor and fuselage-wake interference at almost no extra cost within comprehensive rotor codes.

The purpose of usage is within comprehensive rotor codes such as CAMRAD II, DLR's S4 or similar. Two applications are considered for this model:

a. Blade element aerodynamics: modification of local angle of attack and dynamic pressure.

b. Rotor wake: prescribed or free-wake perturbations due to fuselage presence.

The first application will modify blade loading, especially in fast flight since the fuselage-induced velocities scale with flight speed. They will change rotor thrust and moments and thus trim control angles. The second application will modify the wake geometry according to the fuselage influence. Results found by using this model are (angle of attack variations only):

a. Effect on thrust (or collective control): The mean value of fuselage-induced velocities is about zero for zero angle of attack, thus the impact on thrust or collective to re-trim thrust is about zero as well. Nose-down (negative) angles of attack cause an upwash in average and thus a thrust increase, or smaller collective to re-trim the rotor; nose-up (positive) angles act opposite. The effect is essentially linear in advance ratio and non-linear in angle of attack.

b. Lateral cyclic control: The upwash in the front half of the disk, combined with the downwash in the rear half of the disk, requires large lateral cyclic control angles up to $1°$ and more to re-trim the rotor. The effect is essentially linear in advance ratio and non-linear in angle of attack. In the extremes, when $\alpha = \pm 90°$, the fore-aft asymmetry almost vanishes (upwash or downwash everywhere with only little fore-aft imbalance).

c. Longitudinal cyclic control: Compared to the lateral control the fuselage effect on longitudinal control is much less. This is due to the lateral symmetry of the fuselage-induced velocitiy field. The effect is essentially quadratic in the advance ratio and non-linear in angle of attack; it vanishes for $\alpha = \pm 90°$ because then no difference in dynamic pressure on the advancing and retreating side exists any more.

The impact of fuselage-induced flow on rotor trim asymptotically decays with increasing distance of the rotor to the fuselage. About three rotor radii are sufficient to ignore the effects. In side-slip operating conditions, up to quartering flight, the fuselage-induced flow field is no longer laterally symmetric and thus increasingly affects the longitudinal control with increasing side-slip angle, while the impact on the lateral control simultaneously is reducing.

Future studies using wake deformation due to the fuselage may investigate this effect on blade-vortex interaction (BVI) locations and thus rotor noise radiation, but this effect is assumed to be minor since these BVI locations are at lateral positions farer away of the fuselage where the fuselage-induced velocities are rather small and therefore the wake perturbations as well.

8. REFERENCES

[1] Yamauchi G K, and Johnson W. Analysis of axisymmetric body effects on rotor aerodynamics using modified slender body theory. *Proc. AIAA 2nd Applied Aerodynamics Conference*, Seattle, WA, Aug. 21-23, 1984.

[2] Sheridan P F, and Smith R P. Interactional Aerodynamics - a New Challenge to Helicopter Technology. *J. Am. Helicopter Soc.*, Vol. 25, No. 1, pp 3-21, 1980.

[3] Stepniewski, W Z, and Keys C N. *Rotary-Wing Aerodynamics*. Dover Publications, 1984.

[4] Huber H, and Polz G. Studies on Blade-to-Blade and Rotor-Fuselage-Tail Interferences. *Aircraft Engineering and Aerospace Technology*, Vol. 55, No. 10, pp 2-12, 1983.

[5] van der Wall B G, Bauknecht A, Jung S N, and You Y H. Semi-Empirical Modeling of Fuselage-Rotor Interference for Comprehensive Codes: The Fundamental Model. *CEAS Aeronautical Journal*, Vol. 5, No. 4, pp 387-401, 2014.

[6] Dreier M E**.** *Introduction to Helicopter and Tiltrotor Flight Simulation*. AIAA Education Series, 2007.

[7] Leoni R D. *Black Hawk: The Story of a World Class Helicopter.* AIAA Library of Flight, 2007.

[8] van der Wall, B.G., Jung, Sung N., Rajagopalan, G., Solis, E. Castro, A.: Fuselage-Induced Velocity Model for LRTA, RTA, and HART Fuselages. Report NASA/CR-2015-218840, Moffett Field, CA, 2015.

[9] Gerhold T, Galle M, Friedrich O, and Evans J. Calculation of Complex Three-Dimensional Configurations Employing the DLR-TAU-Code, *Proc. 35th AIAA Aerospace Sciences Meeting & Exhibit*, Reno, NV, Jan. 6-9, 1997.

[10] Rajagopalan R G, Baskaran V, Hollingsworth A, Lestari A, Garrick D, Solis E, and Hagerty B. RotCFD, a Tool for Aerodynamic Interference of Rotors: Validation and Capabilities. *Proc. AHS Future Vertical Lift Aircraft Design Conference*, San Francisco, CA, Jan. 18-20, 2012.

[11] Kim J W, Park S H, and Yu Y H. Euler and Navier–Stokes simulations of helicopter rotor blade in forward flight using an overlapped grid solver. *Proc. 19th AIAA CFD Conference*, San Antonio, TX, June 22–25, 2009.

APPENDIX

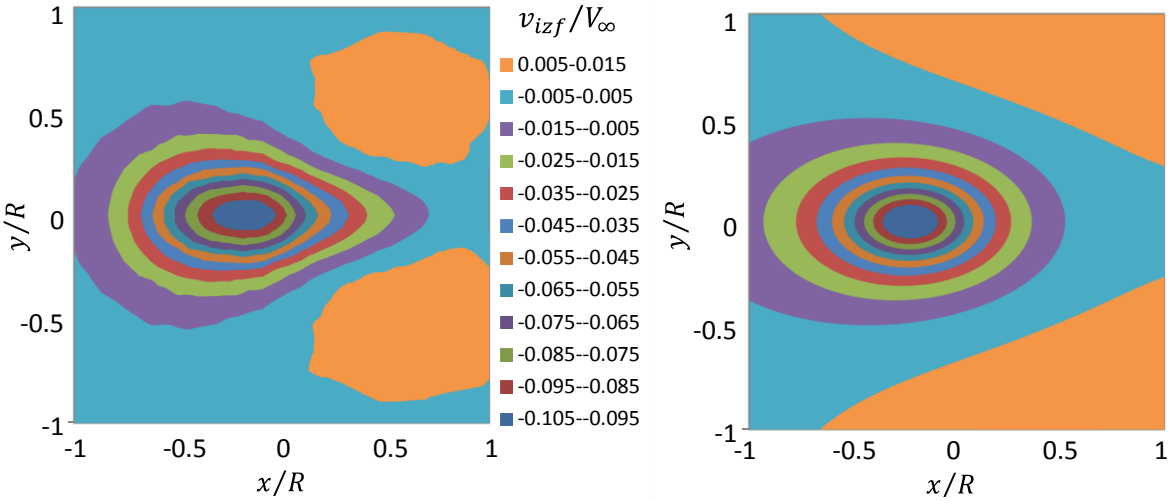

(a) LRTA: CFD data (left), model (right), $\alpha = -20°$

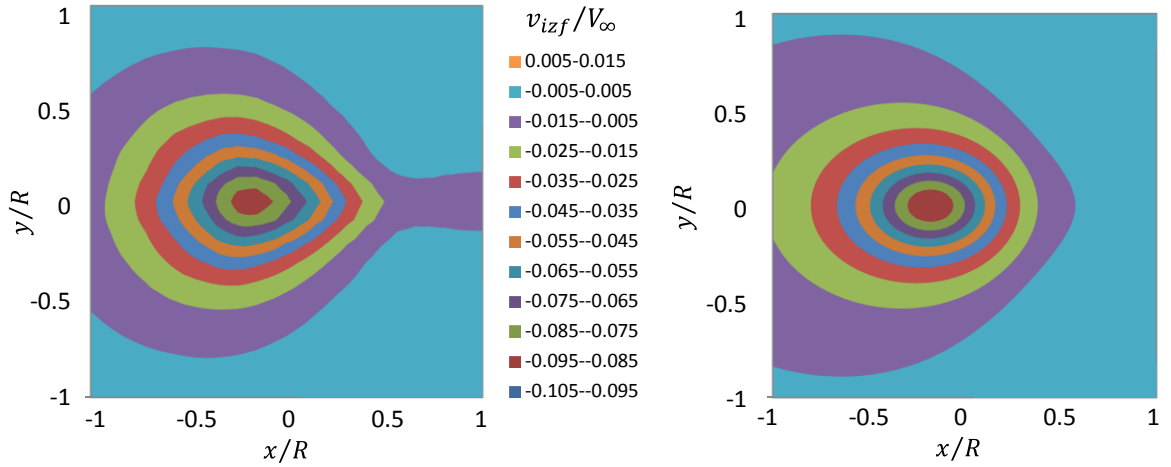

(b) RTA: CFD data (left), model (right), $\alpha = -20°$

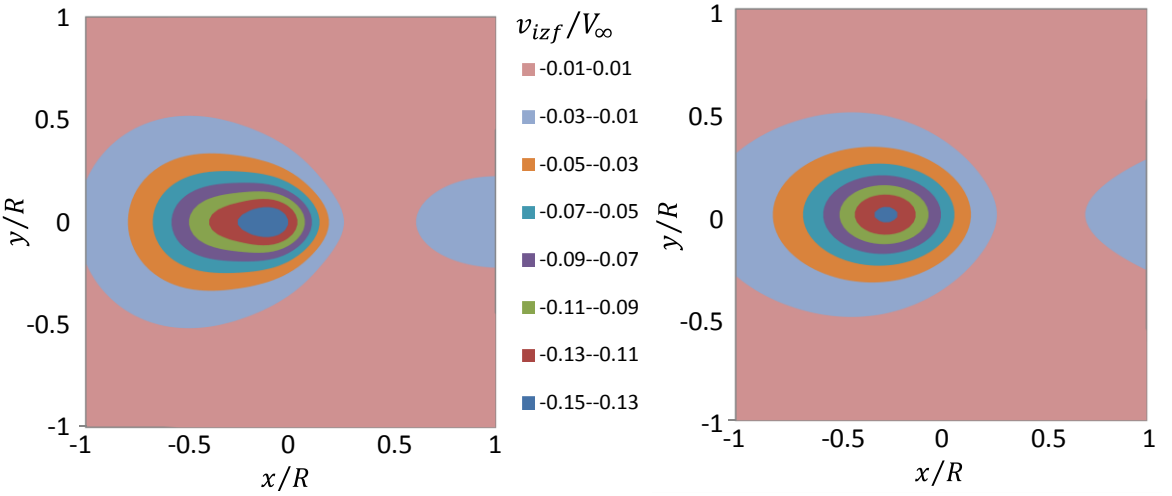

(c) HART: CFD data (left), model (right), $\alpha = -30°$

Fig. 21. Comparison of CFD data with the model, nose-down α, $z/R = 0.1$.

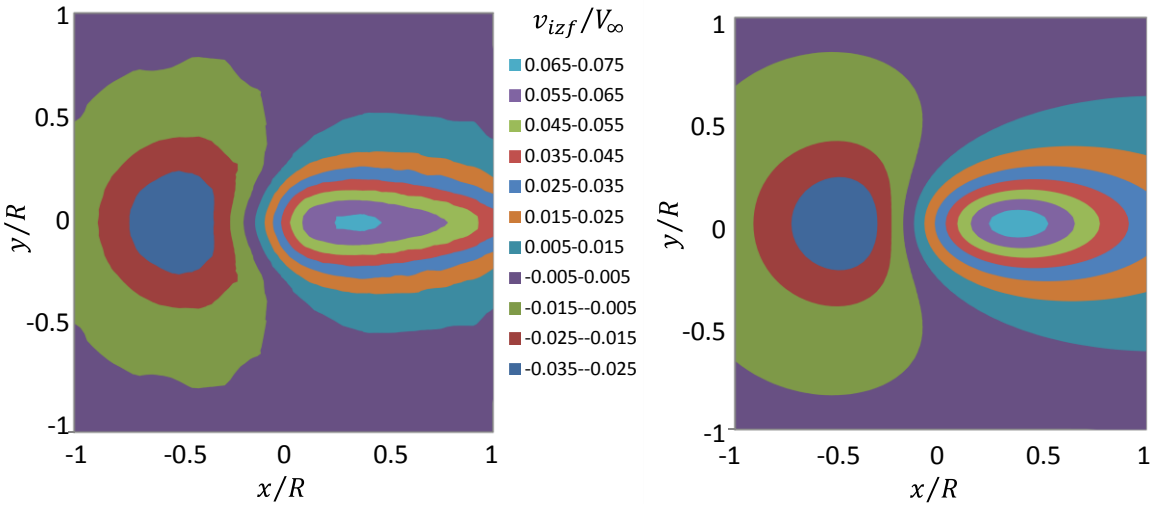

(a) LRTA: CFD data (left), model (right)

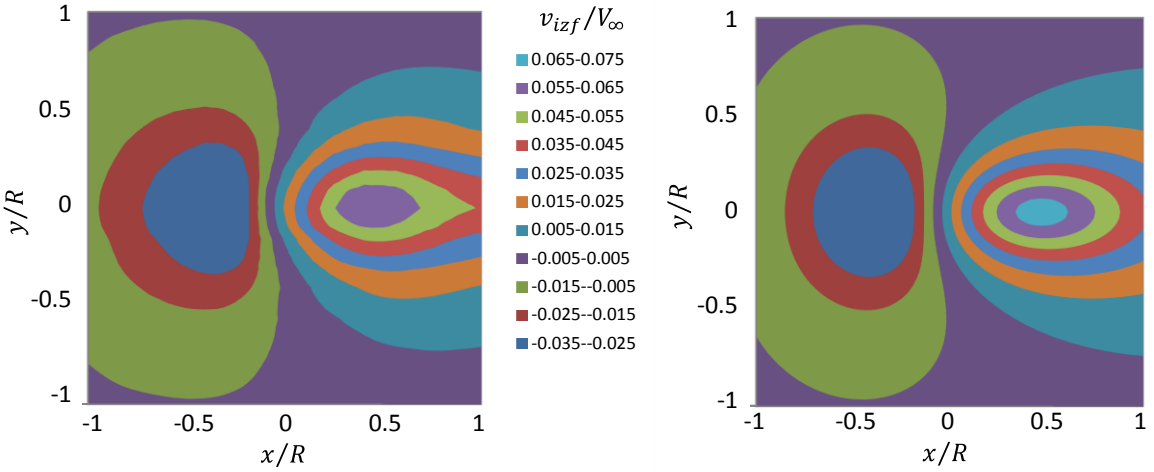

(b) RTA: CFD data (left), model (right)

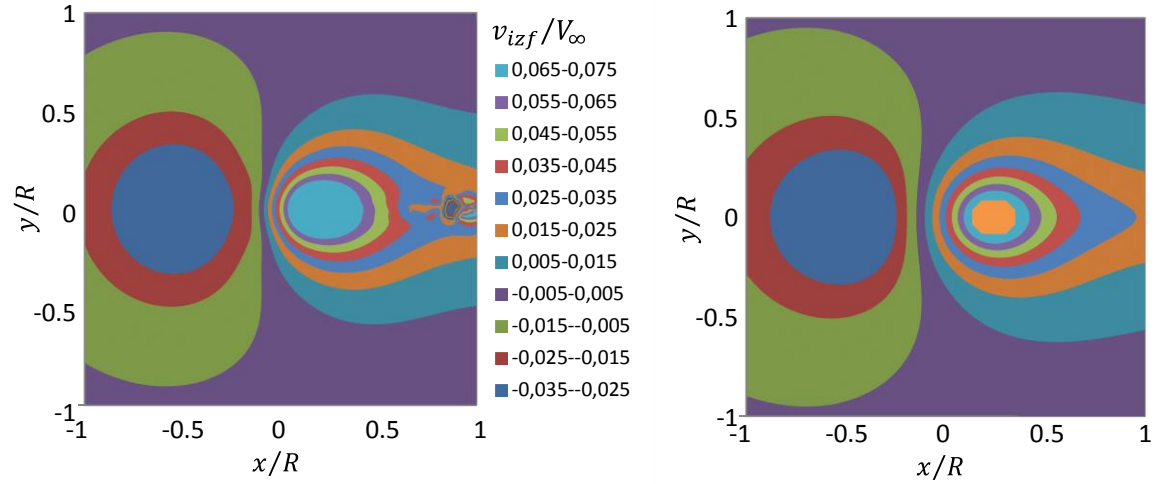

(c) HART: CFD data (left), model (right)

Fig. 22. Comparison of CFD data with the model, $\alpha = +10°,\ z/R = 0.1$.